ENVIRONMENTAL RESEARCH
LETTERS

LETTER • OPEN ACCESS

Remote climate change propagation across the oceans—the directional swell signature

To cite this article: Gil Lemos *et al* 2021 *Environ. Res. Lett.* **16** 064080

ENVIRONMENTAL RESEARCH
LETTERS

LETTER

Remote climate change propagation across the oceans—the directional swell signature

Gil Lemos[1,*], **Alvaro Semedo**[1,2], **Mark Hemer**[3], **Melisa Menendez**[4] and **Pedro M A Miranda**[1]

[1] Instituto Dom Luiz (IDL), Faculdade de Ciências, Universidade de Lisboa, Campo Grande, 1749–016, Lisboa, Portugal
[2] IHE Delft, Department of Coastal, Urban Risk and Resilience, Westvest 7, 2611 Delft, The Netherlands
[3] CSIRO Oceans and Atmosphere, Hobart, TAS, Australia
[4] Environmental Hydraulics Institute 'IH Cantabria', Universidad de Cantabria, Santander, Spain
[*] Author to whom any correspondence should be addressed.

E-mail: grlemos@fc.ul.pt

Keywords: remote, climate change, propagation, swell, waves

Supplementary material for this article is available online

OPEN ACCESS

RECEIVED
18 March 2021

REVISED
7 May 2021

ACCEPTED FOR PUBLICATION
24 May 2021

PUBLISHED
14 June 2021

Abstract

The energy content of wind-waves is propagated across the oceans in the form of swell waves, the main drivers of long-term changes in coastal morphology and offshore hazards. A state-of-the-art swell tracking algorithm is applied to a global ensemble of CMIP5 dynamic wave climate projections, to assess future changes in remotely originated swell events towards the end of the 21st century, and how they propagate. The contribution of multiple wave generation areas is considered. It is found that the projected climate change signal is effectively propagated from the winds along the extratropical storm tracks to remote locations, in the tropical and subtropical latitudes, through swell waves. The statistically significant projected changes in swell wave heights and swell predominance at the remote swell arrival locations are comparable with the ones at the wave generation areas. Furthermore, different incoming directions for swell events at remote locations are shown to often carry opposite climate change signals, propagated from different remote origins. These results highlight the need for a directional approach on wave climate projections, critical for improved vulnerability assessments and adaptation measures from the climate community.

1. Introduction

Winds blowing over the ocean surface are responsible for the generation of wind-waves. These, dominate the ocean wave spectrum, exceeding the energy contribution of tides, tsunamis, and other ocean waves (Kinsman 1965). Wind-waves (henceforth just 'waves') have a clear impact on coastal processes (Toimil *et al* 2019), such as coastal erosion and accretion (Ranasinghe *et al* 2016), defining sediment budgets and shoreline stability (Barnard *et al* 2015). They also impact on offshore infrastructures and shipping design standards (Bitner-Gregersen *et al* 2015), being a major hazard to any operation at sea.

Due to their dispersive nature, locally and remotely generated waves coexist at the ocean surface, classified as wind-sea or swell. The dimensionless wave age parameter (Jeffreys 1924, 1925; see section 2) is commonly used to characterize the wave field, as dominated by wind-sea or swell waves. It is defined as the relative speed between the peak wave and the overlaying wind, the wave field being considered dominated by wind-sea (swell) if the value is below (above) 1.2. While wind-sea waves are strongly coupled to the local wind field, swells propagate freely from their generation area, detached from overlaying winds. Since swell waves dominate the open ocean (Semedo *et al* 2011), local wind and wave fields often do not reflect each other. However, since swell energy is mostly preserved on propagation (Munk *et al* 1963, Snodgrass 1966, Ardhuin *et al* 2009, Semedo *et al* 2009, Pérez *et al* 2014), changes in swells at a certain remote location end up reflecting changes in remote wind energy input at the wave generation area.

Projecting future changes in swell characteristics is of paramount importance for coastal and offshore

climate change adaptation and mitigation policies, particularly in areas exposed to more than one dominant incoming wave direction, vulnerable to the disproportionate effects from changes in swell regimes (Alves 2006), which might aggravate other impacts of climate change such as sea-level rise. In the open ocean, swells also have an impact on the lower marine atmospheric boundary layer (MABL; Smedman *et al* 1999, Sullivan *et al* 2008, Semedo *et al* 2009), by inducing a reverse momentum flux from the ocean surface to the atmosphere (upwards), generating the so-called 'wave-driven wind' (Harris 1966). Under swell influence (typically for wave age values greater than 1.2), the wind profile often shows a low-level wind maximum, close to the surface, followed by a negative (or constant) vertical wind gradient, extending the impact of swells into the lower troposphere by collapsing the MABL turbulence structure (Semedo *et al* 2009). Grachev and Fairall (2001) showed, based on observations, that the momentum flux should only occur at high wave age values (between 5 and 20), but field measurements by Smedman *et al* (1999) and Smedman *et al* (2009) concluded that swell waves can actually have a strong impact on the MABL structure even at lower wave ages.

In this study, a swell-tracking algorithm developed by Portilla (2012) and upgraded by Amores and Marcos (2019), is applied to a global dynamic ensemble of CMIP5 wave climate projections. The algorithm isolates swell events from the remaining local sea state conditions, based on the behavior of the peak wave period (T_p) and peak mean wave direction (MWD_p). Since lower-frequency waves are the first to arrive to a remote location, followed by higher-frequency ones, the algorithm exploits the condition that wave frequency and time of arrival are related in a *quasi*-linear fashion, allowing to establish a time of travel and a distance to the wave generation site. By applying a modified version of the algorithm, to improve the representation of uncertainties (see section 2), global 21st century mean significant wave height (H_S) projections, exclusively associated to swell events subjected to projected changes in close to surface wind speeds (U_{10}) at the wave generation areas, are presented. Our goal is twofold. First, to assess how the climate change signal propagates through swell waves, from the overlaying winds at the wave generation areas to the swell arrival locations. Second, to highlight the relevance of considering the specific directional features in wave climate projections, usually overlooked in conventional studies centered on bulk wave parameters, integrated for all incoming directions.

The remainder of the paper is structured as follows: in section 2, the data sets and methodologies are presented. In section 3, the projected changes in swell events characteristics are assessed, highlighting the propagation of climate change through swells. Conclusions are presented in section 4.

2. Data and methods

2.1. The climate simulations

A seven-member CMIP5 multi-forcing multivariate dynamic wave climate ensemble is used. Three hourly U_{10} and monthly sea ice concentration from seven different General Circulation Models (GCMs) were used to force the WaveWatchIII (WW3) wave model (version 3.14; Tolman 2009). WW3 was setup with the BAJ-ST3 parameterization, adapted from Bidlot *et al* (2005), and implemented over a global $1^\circ \times 1^\circ$ horizontal grid. Further details in table SM1 and Hemer and Trenham (2016). The 6 hourly H_S, T_p and MWD_p wave parameters were used, at $1^\circ \times 1^\circ$ resolution. The atmospheric component of the ensemble (U_{10}), the wave climate simulations forcing fields, were interpolated to $2^\circ \times 2^\circ$, so that all ensemble members share the same horizontal resolution. The wind and wave climate simulations were divided into present (1986–2005; PC20) and future climate (2081–2100; FC21), following the RCP8.5 scenario (Riahi *et al* 2011). Ensemble means in figures 2(a) and (b) were determined considering an unweighted mean of the individual members.

2.2. The swell tracking algorithm

The identification of swell events followed the algorithm developed by Portilla (2012) and upgraded by Amores and Marcos (2019). It determines the traveling distance and time for each swell event, taking into consideration the waves dispersive properties. For waves propagating in deep waters, their phase speed (c_p) is given by equation (1), where g corresponds to the gravity acceleration and f_p to the peak wave frequency:

$$c_p = \frac{g}{2\pi f_p}, \tag{1}$$

therefore, lower frequency waves travel faster than higher frequency ones. Assuming waves generated by the same storm and traveling along great circles, the distance (d; equation (2)) and time of travel (t_0; equation (3)) for one or several wave groups can be computed as:

$$d = \frac{g}{4\pi}\frac{\partial t}{\partial f_p}, \tag{2}$$

$$t_0 = \frac{\partial\left(T_p t\right)}{\partial T_p}. \tag{3}$$

Geographical constraints, such as islands and atolls, can shelter swells and affect their characteristics, leading to potential changes in wave heights and directions. For that matter additional steps were proposed by Amores and Marcos (2019) to deal with the presence of obstacles along wave trajectories, and isolate pure swell events, undisturbed from their origin to their arrival locations. The algorithm was applied at

each 2° × 2° ensemble grid-point. To avoid sudden T_p variations, resulting from the wave model's frequency discretization, the T_p time-series were smoothed, and the following conditions were applied:

- An abrupt increase in T_p, of at least 1 s in 6 h, marks the beginning of the swell events. T_p values must always be greater than 8 s.
- After the beginning of the swell event, $\partial T_p/\partial t$ must be negative, however, T_p must not decrease too fast, to avoid mixing with different wave groups: $\partial T_p/\partial t \geqslant -2$ s/6 h. For the same reason, $\Delta MWD_p \leqslant 10°$.
- Swell events must last at least 24 h.

d and t_0 were obtained by computing a linear regression during the entire duration of the swell events. The respective 95% confidence intervals were defined, and events were excluded when the relative error between the upper and lower ones exceeded 30%. Events with trajectories over land were also excluded. The H_S (U_{10}) mean conditions inside a 3° × 3° (2° × 2°) domain, for 48 h centered on the time of origin, were used as conditions at origin, to account for the uncertainty related to the confidence intervals and MWD_p discretization.

2.3. The wave age parameter

The wave age parameter (χ_{10}), developed by Jeffreys (1924, 1925) is defined as the peak phase speed, divided by the wind speed, as equation (4):

$$\chi_{10} = \frac{c_p}{U_{10}}. \tag{4}$$

The 'age' of the waves is closely related to the fundamentals of air-sea interaction, specifically to the transition between wind sea and swell dominated wave fields, and to the feedbacks from waves to the atmosphere, and its subsequent impact in the MABL. Further details can be found in Grachev and Fairall (2001), Högström *et al* (2009), Semedo *et al* (2009, 2012) and Rutgersson *et al* (2009). A swell dominated wave field occurs when $\chi_{10} > 1.2$. The impact of a swell dominated wave field in the atmosphere, giving rise to wave driven wind maxima (jets), including the reversal momentum flux, is maximized for $\chi_{10} > 5$ (Högström *et al* 2009, 2015).

2.4. Projected changes and statistical significance

A total of 4582773 swell events were selected during PC20, and 5367598 during FC21, corresponding to a projected increase of 17.1%. After selection, the associated parameters were re-gridded into 2° × 2° cells. Weighted means were computed for each parameter (X) inside each cell, as in equation (5), based on the relative errors obtained for d and t_0. A weight (w) of 1 (0.1) was attributed to the swell event with the lowest (highest) errors, linearly decreasing with increasing errors:

$$\bar{X} = \frac{\sum_{i=1}^{N} X_i w_i}{\sum_{i=1}^{N} w_i}. \tag{5}$$

A minimum of 20 events per cell was established, to compute the swell-related statistics in figures 3–5. In figures SM1–SM5 (available online at stacks.iop.org/ERL/16/064080/mmedia), however, all swell events were considered. Statistical significance of the projected changes was computed using a *t-test* for difference in means. The dots in figures 3–5 correspond to statistically non-significant areas, at the 90% confidence level. In figure 2, stippling refers to areas with at least two statistically non-significant members (out of 7). Projected changes are shown as normalized differences: FC21 minus PC20, normalized by PC20 (in %).

2.5. Wave generation areas

Five wave generation areas were selected along the extratropical latitudes of both hemispheres. These correspond to the common areas where a minimum of 200 swell events are originated, under at least −1% (Northern Hemisphere) and 1% (Southern Hemisphere) mean wind speed ($\overline{U_{10}}$, where the bar denotes 'mean') projected change. This threshold ensured that all waves departing from each generation area were originated under similar conditions, thus allowing to explore the propagation of the climate change signal. The areas were named as: NPAC (North Pacific), SPAC (South Pacific), NATL (North Atlantic), SATL (South Atlantic) and SIND (South Indian). Projections for the number of events in figures SM1–SM5 (crosses and dots) were computed considering only the areas with more than 200 events (thus addressed to as 'meaningful'). The number of swell events is denoted as N, such as: N^{OR} at origin (at the wave generation areas) and N^{ARR} at arrival. Likewise, the $\overline{H_S}$ exclusively associated to swell events is denoted as $\overline{H_S^{OR}}$ at origin and $\overline{H_S^{ARR}}$ at arrival.

2.6. Evaluation

An evaluation of the ensemble presented here, under a similar algorithm, in comparison with a wave hindcast, was presented in Amores and Marcos (2019). Their results showed the ensemble's ability to simulate swell events arriving at the global coastlines, despite a slight $\overline{H_S^{ARR}}$ underestimation.

3. Results

Five wave generation areas were selected, as the most likely origin of swell events in present climate, under $\overline{U_{10}}$ projected changes (see section 2 and figure 2(a)). 19.4% of all global present climate swell events are generated at SPAC, followed by SIND (19.2%), SATL (14.2%), NPAC (8.43%) and NATL (2.44%). The

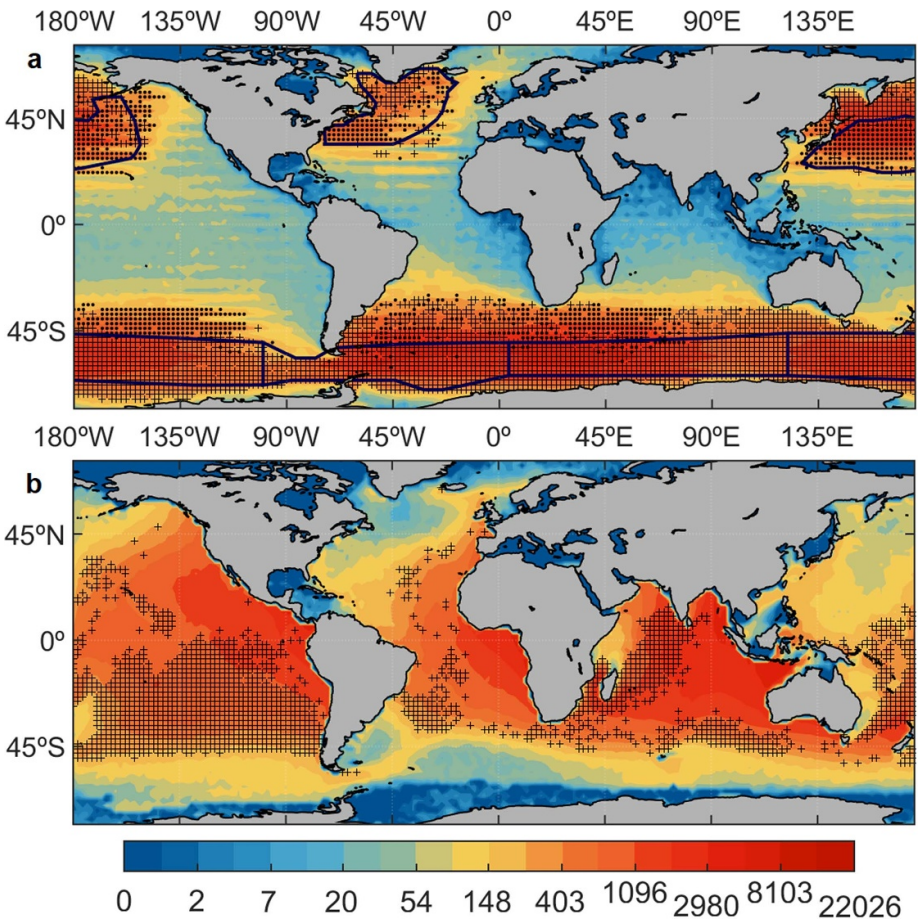

Figure 1. Global swell events' a, N^{OR}_{PC20} and b, N^{ARR}_{PC20}, and meaningful (see section 2) projected changes (FC21 *vs* PC20), above 20% (crosses) and below −20% (dots).

future projected ranking is similar but shows a greater contribution of the Southern Hemisphere (SH) to the global swell climate, having SPAC generating 22.9% of all events, followed by SIND (19.6%), SATL (15.5%), NPAC (6.52%) and NATL (1.96%). The combined contribution of the five areas corresponds to about 63.7% (66.4%) of N_{PC20} (N_{FC21}). Figure 1(a) shows that meaningful N^{OR}_{PC20} (see section 2) projected changes, above 20%, occur essentially at the SH high latitudes (below −20% in the mid latitudes), possibly due to the projected poleward shift of the extratropical storm tracks, by the end of the 21st century (Bengtsson *et al* 2009, Wu *et al* 2010, Arblaster *et al* 2011, Tamarin and Kaspi 2017). This is noticeable as well in the Northern Hemisphere (NH). The eastern halves of the three major ocean basins ('swell pools'; Chen *et al* 2002) correspond to the most likely swell arrival locations (figure 1(b)). Meaningful N^{ARR}_{PC20} projected increases at arrival, above 20%, dominate the tropics and subtropics, especially in the SH.

At NPAC and NATL, statistically significant projected decreases in $\overline{U_{10}}$ are visible, down to −5.44% and −7.24%, respectively (figure 2(a)). On the other hand, for SPAC, SATL and SIND, $\overline{U_{10}}$ projections show a statistically significant expected increase, peaking at 6.67%, 6.29% and 9.20%, respectively. The total $\overline{H_S}$ (combined wind sea and swell) projected changes (figure 2(b)) follow the $\overline{U_{10}}$ patterns where greater wind-sea contribution is present (namely inside the selected wave generation areas), being detached where swells prevail. Since the total $\overline{H_S}$ accounts for all directions and frequencies at each grid-point, the associated projections are often flattened, especially in areas where swell waves from different origins coexist, carrying distinct climate change signals. To highlight the advantages of considering specific incoming directions in $\overline{H_S}$ projections, three recurrent swell-arriving locations, roughly in the center of each ocean basin (and in the vicinity of populated archipelagos, namely the Hawaii, the Azores and the Maldives), were selected (figure 2(b)), allowing, at the same time, to locally quantify the propagation of climate change propagation, through swells, from different generation areas.

Projections of $\overline{H^{OR}_S}$ (i.e. of the $\overline{H_S}$ associated to the swell events at the selected wave generation areas), in figures 2(b), (e), 3(b), (e) and 4(b) show close resemblance to the $\overline{U_{10}}$ (figures 2(a), (d), 3(a), (d) and 4(a)) and total $\overline{H_S}$ ones (figure 2(b)), due to the strong coupling between wind and wave behavior there (typical when wind sea dominates over swell). NPAC swell events radiate eastwards and southwards, affecting

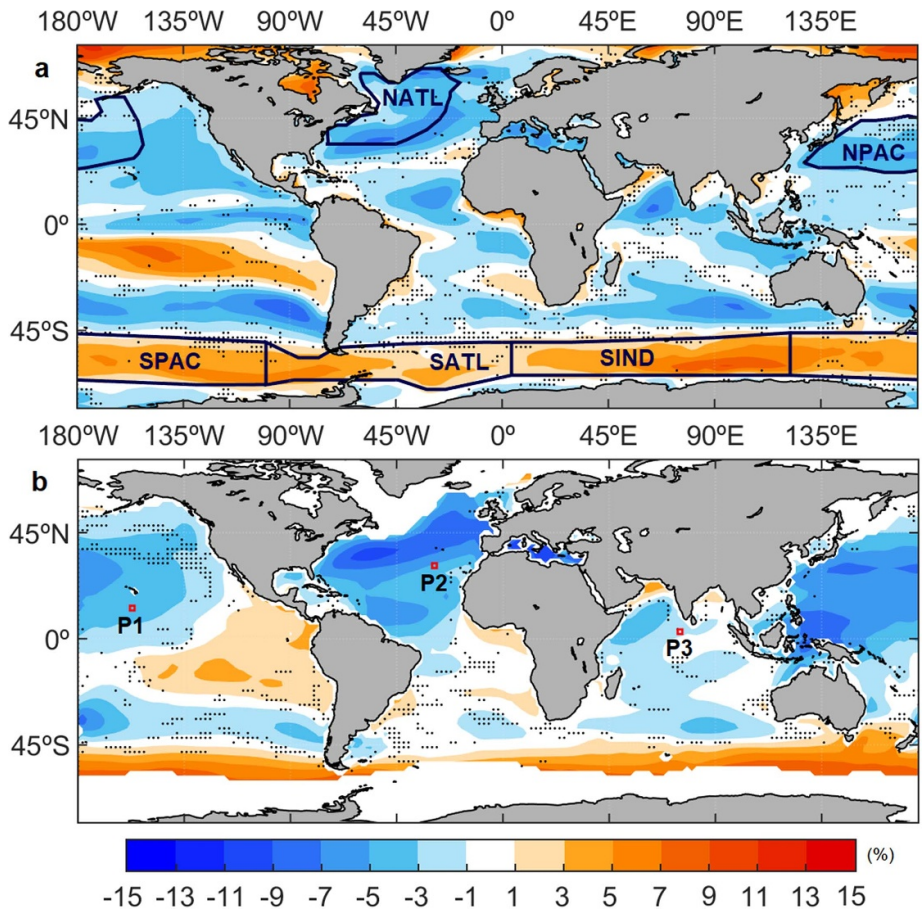

Figure 2. (a) Ensemble $\overline{U_{10}}$ projected changes, selected generation areas and corresponding acronyms. (b) Ensemble total $\overline{H_S}$ projected changes and P1, P2 and P3 locations. Stippling denotes areas without statistical significance at the 90% confidence level (see section 2).

the Central and Eastern Pacific tropical and subtropical areas. N_{PC20}^{ARR} projected changes below −20% are visible there, suggesting less events from NPAC arriving to the tropical Pacific in the future (figure SM1). SPAC events show not only a wider area of propagation, covering most of the Eastern Pacific, as far as the coasts of Alaska, but also broader N_{PC20}^{ARR} projected increases, exceeding 20% in most of the area (figure SM2), including along the coasts of North and South America.

Considering the events originated at NPAC, 8.99% (36.6%) of the swell arrival locations show statistically significant $\overline{H_S^{ARR}}$ projected increases (decreases). NPAC $\overline{H_S^{ARR}}$ decreases can be expected mostly in the Central Pacific (figure 3(c) and table 1), the same region where a lower number of NPAC events are projected to arrive at (figure SM1). Events coming from the SPAC, on the other hand, show statistically significant $\overline{H_S^{ARR}}$ projected increases (decreases) in 35.8% (9.31%) of their area of effect, being increases dominant throughout most of the tropical and subtropical Pacific (figure 3(f)), as far as the southern coasts of California. $\overline{H_S^{ARR}}$ follows quite reasonably the behavior of $\overline{H_S^{OR}}$ (figures 3(b), (e) and ultimately $\overline{U_{10}^{OR}}$; figures 3(a) and (d)), especially when statistical significance is included, stressing the dependency of swells characteristics on their generation area. In fact, table 1 shows that the NPAC $\overline{U_{10}^{OR}}$ and $\overline{H_S^{OR}}$ (averaged for the entire area) are projected to decrease 3.2% and 4.8%, respectively, being the $\overline{H_S^{ARR}}$ (averaged for all NPAC originated events) also expected to decrease 2.7%. Likewise, SPAC averaged $\overline{U_{10}^{OR}}$, $\overline{H_S^{OR}}$ and $\overline{H_S^{ARR}}$ are projected to increase 2.9%, 5.0% and 2.9%, respectively.

At P1 location, South of Hawaii (figure SM7), most of the arriving PC20 swells are generated at NPAC (193 events, or 22.2% more than at SPAC; table 2). Enhanced southerly swell prevalence, combined with fewer northerly events, is expected to reverse this balance in the future, with SPAC contribution surpassing NPAC in 25.3% (213 events *versus* 170). Figure 2(b) shows that the total P1 $\overline{H_S}$ is projected to decrease (−4.15%; table 2). However, opposite $\overline{H_S^{ARR}}$ projections are visible there (figures 3(c)and (f)), ranging from −8.25% for the northerly events (NPAC) to 3.96% for the southerly ones (SPAC), being the difference similar for the mean above the 90% percentile (−9.06% to 3.18%, respectively; table 2). P1-related $\overline{H_S^{OR}}$ and $\overline{U_{10}^{OR}}$ projections agree with the $\overline{H_S^{ARR}}$ ones, indicating

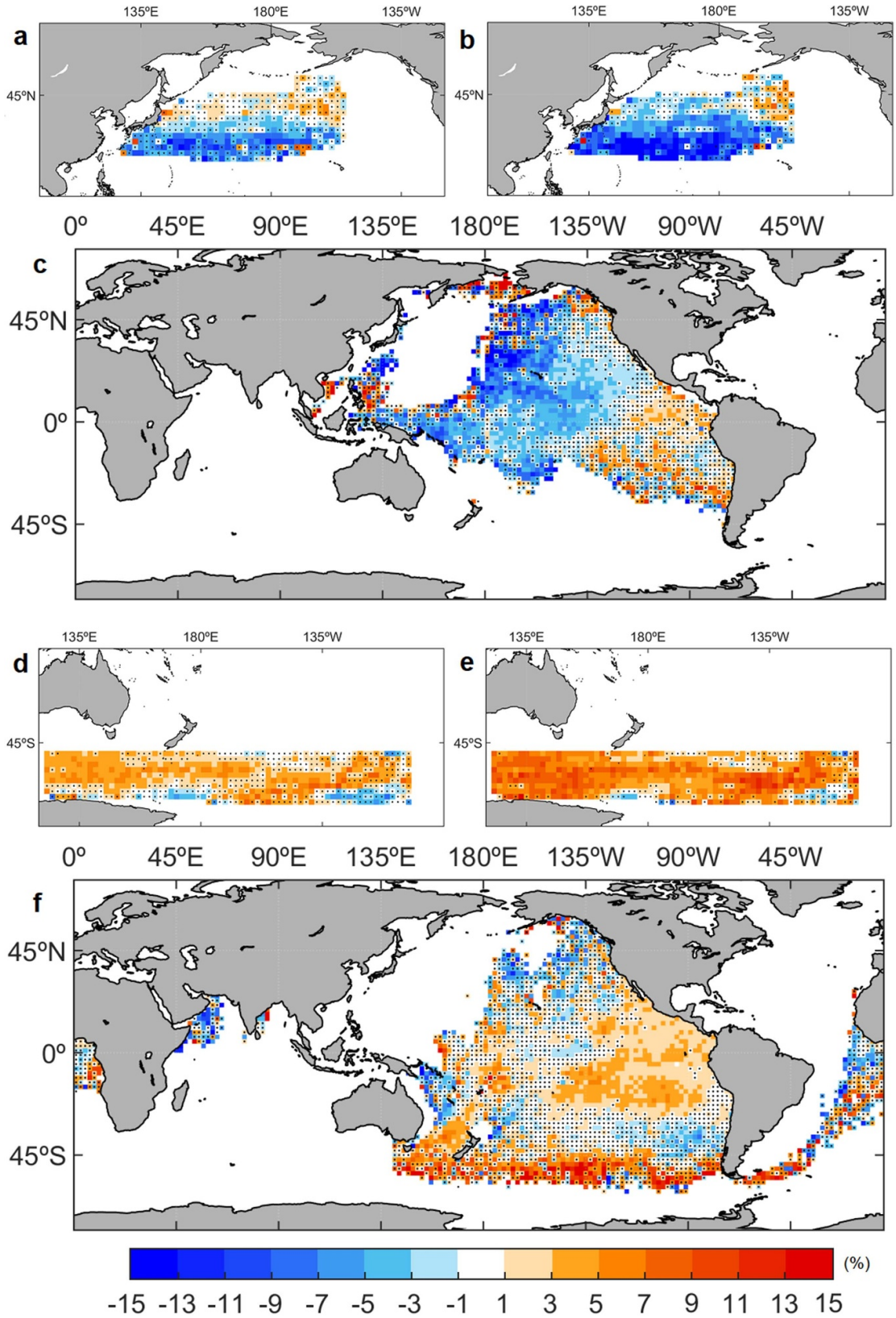

Figure 3. $\overline{U_{10}^{OR}}$ projected changes (FC21 *vs* PC20; in %) at (a) NPAC and (d) SPAC. $\overline{H_S^{OR}}$ projected changes at (b) NPAC and (e) SPAC. $\overline{H_S^{ARR}}$ projected changes for events generated at (c) NPAC and (f) SPAC. Dots denote areas without statistical significance at the 90% confidence level.

propagation of climate change signal through swells: projected decreases at NPAC (−3.47% and −1.95%, respectively), and projected increases at SPAC (4.36% and 1.88%, respectively), with greater gaps for the upper percentiles. Additionally, projected increases in $\overline{\chi_{10}}$ (figure SM6a) and extreme χ_{10} frequency (figure SM6b) in most of the Pacific indicate a potentially higher swell influence on the MABL, with

Table 1. PC20 and FC21 $\overline{H_S^{ARR}}$ (m), $\overline{H_S^{OR}}$ (m) and $\overline{U_{10}^{OR}}$ (m s^{-1}) considering the entire swell generation areas and respective arrival areas (under the threshold $N^{ARR} > 20$), and percentage of these areas showing statistically significant (SS) projected changes, together with the percentage covered by positive (+) or negative (−) ones.

	NPAC	SPAC	NATL	SATL	SIND
$\overline{H_S^{ARR}}$ PC20	1.86	2.07	1.40	2.06	2.13
$\overline{H_S^{ARR}}$ FC21	1.81	2.13	1.34	2.08	2.15
$\overline{H_S^{OR}}$ PC20	3.33	4.01	2.94	3.26	3.97
$\overline{H_S^{OR}}$ FC21	3.17	4.22	2.80	3.40	4.13
$\overline{U_{10}^{OR}}$ PC20	9.52	10.5	9.65	9.49	10.4
$\overline{U_{10}^{OR}}$ FC21	9.32	10.8	9.32	9.79	10.7
$\Delta\overline{H_S^{ARR}}$ %SS	45.6	45.1	50.6	35.9	39.8
$\Delta\overline{H_S^{ARR}}$ %SS (+)	8.99	35.8	4.53	23.4	14.6
$\Delta\overline{H_S^{ARR}}$ %SS (−)	36.6	9.31	46.1	12.5	25.2
$\Delta\overline{H_S^{OR}}$ %SS	49.5	70.8	36.8	66.5	66.1
$\Delta\overline{H_S^{OR}}$ %SS (+)	1.69	70.5	2.14	65.1	66.1
$\Delta\overline{H_S^{OR}}$ %SS (−)	47.8	0.28	34.7	1.43	0
$\Delta\overline{U_{10}^{OR}}$ %SS	23.2	44.4	20	50.4	48.4
$\Delta\overline{U_{10}^{OR}}$ %SS (+)	2.17	42.4	0.36	49.9	48
$\Delta\overline{U_{10}^{OR}}$ %SS (−)	21.0	1.97	19.6	0.48	0.42

Table 2. Projected changes (Δ; in %) for the $\overline{H_S}$, $\overline{H_S^{ARR}}$, $\overline{H_S^{OR}}$ and $\overline{U_{10}^{OR}}$ (in %) and corresponding means above the 90% percentile at P1 (South of Hawaii), P2 (South of Azores) and P3 (Maldives), considering each of the contributing generation areas with $N^{ARR} > 20$.

	South of Hawaii (P1)		South of Azores (P2)		Maldives (P3)	
$\Delta\overline{H_S}$	−4.15		−4.69		−1.20	
$\Delta\overline{H_S^{ARR}}$	NPAC	−8.25	NATL	−3.78	SATL	3.16
$\Delta\overline{H_S^{ARR}} > P90$		−9.06		−13.1		3.80
$\Delta\overline{H_S^{OR}}$		−3.47		−13.6		8.11
$\Delta\overline{H_S^{OR}} > P90$		−6.60		−10.4		9.36
$\Delta\overline{U_{10}^{OR}}$		−1.95		−9.64		3.77
$\Delta\overline{U_{10}^{OR}} > P90$		−8.09		−7.02		5.32
N_{PC20}^{ARR}		193		217		262
N_{FC21}^{ARR}		170		184		507
$\Delta\overline{H_S^{ARR}}$	SPAC	3.96	SATL	3.71	SIND	−2.47
$\Delta\overline{H_S^{ARR}} > P90$		3.18		13.2		−4.16
$\Delta\overline{H_S^{OR}}$		4.36		3.87		1.93
$\Delta\overline{H_S^{OR}} > P90$		4.01		16.8		−0.27
$\Delta\overline{U_{10}^{OR}}$		1.88		1.57		−0.01
$\Delta\overline{U_{10}^{OR}} > P90$		−1.81		10.5		1.09
N_{PC20}^{ARR}		158		65		921
N_{FC21}^{ARR}		213		114		998

repercussions in lower atmosphere turbulence structure, as part of the waves momentum, originally transferred from the winds during the generation process, is now fed back into the atmosphere, in the form of wave-driven winds.

Despite traceable from the Indian basin, most NATL swell events affect the tropical Atlantic and the eastern North Atlantic (figure SM3). Like NPAC, N_{PC20}^{ARR} projected changes are mostly negative at low latitudes (reaching below −20%), yet localized increases (above 20%) are visible for the European coastlines. Swells originated at SATL show a larger area of propagation, covering the three main ocean basins (figure SM4). In the Atlantic, SATL meaningful N_{PC20}^{ARR} projected increases are visible essentially at the tropical and SH subtropical latitudes, but also in the NH mid latitudes.

Statistically significant $\overline{H_S^{ARR}}$ projected increases (decreases) are visible for NATL events in 4.53% (46.1%) of the arrival area, in the Atlantic tropical and subtropical latitudes (figure 4(c) and table 1). SATL events are less expressive in the Atlantic basin

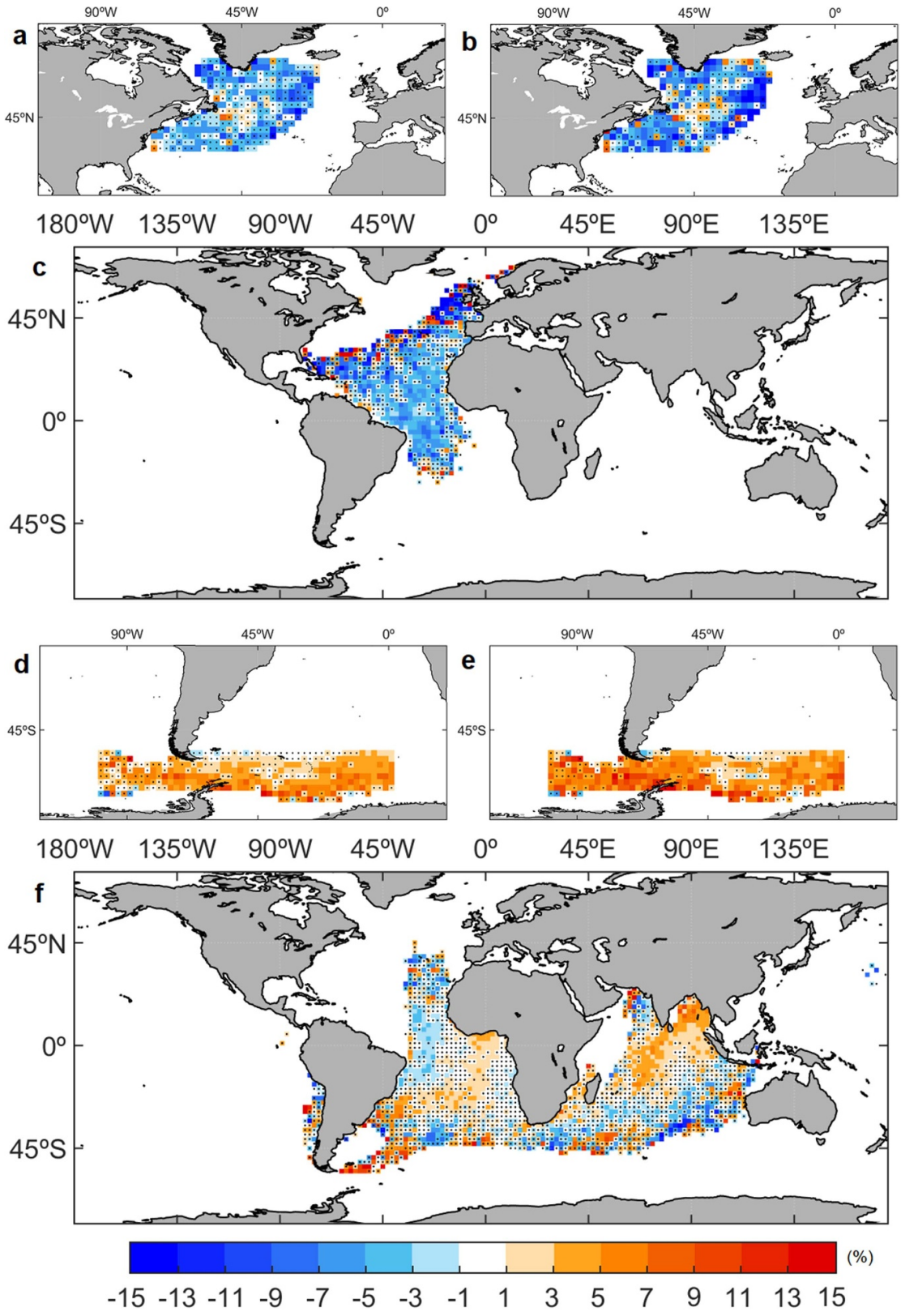

Figure 4. Same as figure 3, but for the NATL and SATL areas.

since a considerable portion propagates to the Indian basin. Nevertheless, statistically significant $\overline{H_S^{ARR}}$ projected increases are visible west of Africa and in the subtropical North Atlantic (figure 4(f)). Overall, 23.4% (12.5%) of the statistically significant $\overline{H_S^{ARR}}$ projections associated to SATL events are positive (negative). Again, these patterns are compatible with the ones for $\overline{H_S^{OR}}$ (figures 4(b) and (e)) and $\overline{U_{10}^{OR}}$ (figures 4(a) and (d)), especially when statistical significance is included (table 1). An increase of the $\overline{\chi_{10}}$

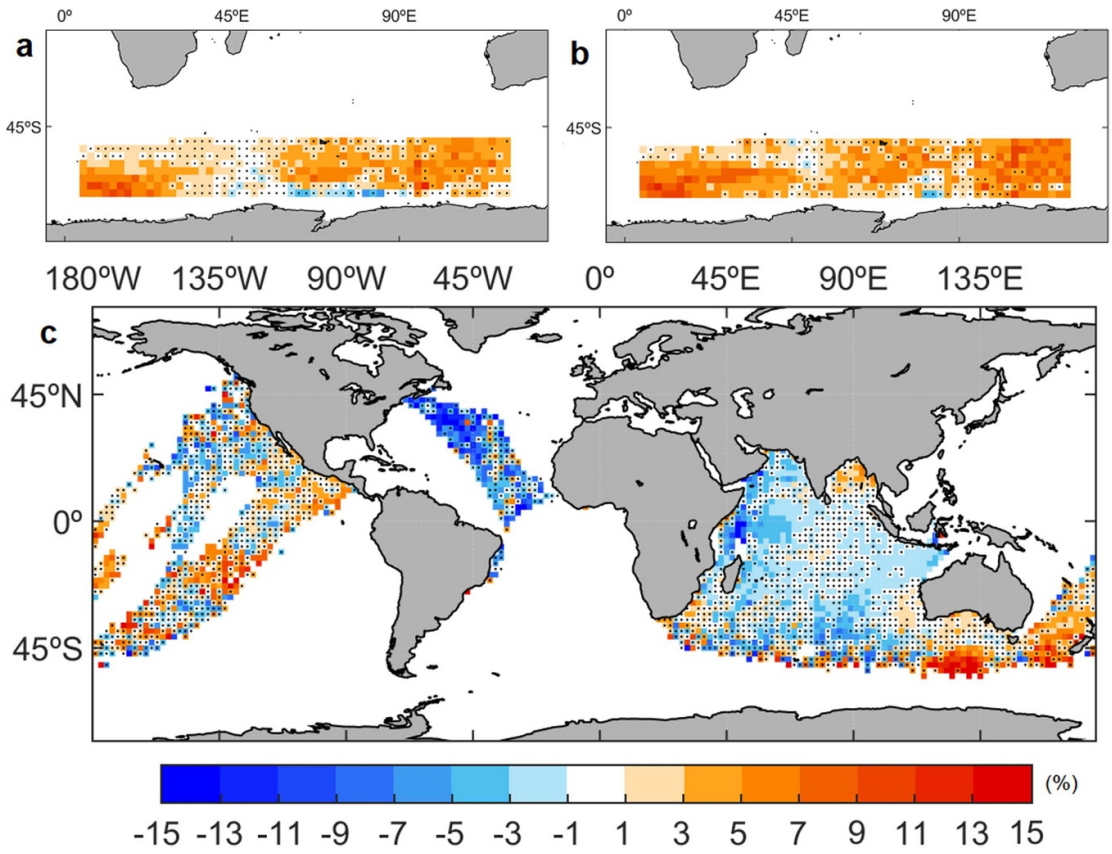

Figure 5. Same as figure 3, but for the SIND area.

can also be expected in the future, throughout most of the Atlantic basin (figure SM6).

At the P2 location, South of the Azores (figure SM7), most of the arriving PC20 swells are generated at NATL (217 events, 234% more than the ones generated at SATL; table 2). In close resemblance to P1, southerly (northerly) swells are projected to become more frequent (scarcer) in the future, reducing the difference to 61.4% during FC21. Despite a total $\overline{H_S}$ projected change of −4.69% at P2 (figure 2(b)), $\overline{H_S^{ARR}}$ projections show, in fact, opposite signals there (figures 4(c) and (f)), ranging from −3.78% for the northerly events (NATL) to 3.71% for the southerly ones (SATL), exacerbated for the mean above the 90% percentile (−13.1% to 13.2%, respectively; table 2). Thus, at P2, while more NATL events are still projected to occur in the future, a weakening of their intensity is expected, in contrast to stronger and more frequent projected swells from SATL. Showing a similar behavior to the $\overline{H_S^{ARR}}$ projections, P2-related $\overline{H_S^{OR}}$ and $\overline{U_{10}^{OR}}$ ones (table 2) indicate that the climate change signal is effectively propagated from wave generation areas, to swell arrival locations.

The SATL area is also responsible for generating a considerable portion of the swell events arriving in the Indian basin (figure SM4), as the second most contributing area there, surpassed just by SIND (figure SM5). High SATL N_{PC20}^{ARR} values are visible at the eastern Indian Ocean along the coasts of Myanmar and Sumatra (Indonesia), comparable to the values in the Gulf of Guinea (Atlantic). While no meaningful change is expected in the areas showing the largest SATL N_{PC20}^{ARR} values in the Atlantic Ocean, SATL N_{PC20}^{ARR} is projected to increase more than 20% throughout most of the Indian Ocean. The area of effect for SIND swell events is also quite extensive (figure SM5). Nevertheless, contrary to SATL, no meaningful N_{PC20}^{ARR} projected changes are expected in the areas where swells arrive more frequently (e.g. the tropical Indian Ocean).

Despite the clear $\overline{U_{10}}$ projected increases at SIND (figure 2(a)), 14.6% (25.2%) of the swell arrival locations for events generated there show statistically significant projected increases (decreases; table 2). In the Indian basin, SIND $\overline{H_S^{ARR}}$ projections are mostly negative, with relatively small statistically significant areas (figure 5(c)). SATL events there, on the other hand, show widespread statistically significant $\overline{H_S^{ARR}}$ projected increases, overlapping with the area of highest N_{PC20}^{ARR} projections (between Madagascar and Myanmar; figure SM4). $\overline{\chi_{10}}$ is also expected to increase, especially in the northern half of the basin (figure SM6).

At the P3 location, near the Maldives (figure SM7), while the contribution of SIND clearly surpasses SATL during PC20 (in 351%; table 2), this gap is expected to be reduced during FC21 (196%), with nearly a doubling of SATL swell events arriving there (from 262 to 507). SIND N_{PC20}^{ARR} is also projected to increase, although marginally (8.36%; from 921 to 998). Thus, it is safe to assume that changes in Maldivian swell climate will be mostly driven by SATL generated events, with a $\overline{H_S^{ARR}}$ projected increase of 3.17% (3.80% for extreme events) at P3, contrasting with the negative projection of −2.47% (−4.16%) for SIND events. Note that the total $\overline{H_S}$ projections at P3 simply show a decrease of −1.20% (figure 2(b)), underrepresenting the effects of waves from specific directions. P3-related behavior at origin shows that SATL and SIND $\overline{H_S^{OR}}$ is projected to increase 8.11% and 1.93%, respectively. $\overline{U_{10}^{OR}}$, however, is projected to increase for SATL (3.77%), and slightly decrease for SIND (−0.01%). The discrepancy between SIND results for P3 (negative $\overline{H_S^{ARR}}$ projection together with a positive $\overline{H_S^{OR}}$ one and a slightly negative $\overline{U_{10}^{OR}}$ one), can indicate that the future strongest SIND swells (associated with projected increases in the westerlies, visible in figures 2(a) and 5(a)) will in fact be pushed towards the Pacific (figure 5(c)), while the weaker ones (associated with local projected $\overline{U_{10}^{OR}}$ decreases; table 2), will more easily be diverted to the center of the Indian basin. The strong eastward component in the direction of propagation of the strongest future swells is also noticeable for SPAC events, some of which arrive in the Atlantic basin (traceable from as far as the Canary Islands), with projected increases of up to 15% (figure 3(f)), and SATL events, which end up in the Indian basin (figure SM4).

4. Conclusions

The behavior of waves associated to swell events under climate change presents a new set of features not previously contemplated in conventional wave climate studies, focused on wave parameters accounted from all incoming directions and frequencies at one place (e.g. Hemer *et al* 2013, Fan *et al* 2014, Lemos *et al* 2019, 2020, 2020b, Morim *et al* 2019). We investigated the propagation of the climate change signal through swell events, as they radiate from their generation area towards remote locations, applying a swell tracking algorithm to a multivariate dynamic ensemble of wave climate projections. Future projected changes in swell-related significant wave heights were shown to be highly linked to the ones at their origin and, therefore, to the main direction of swell propagation.

At the Pacific and Atlantic basins, more frequent (scarcer) southerly (northerly) swells were shown to be expected towards the end of the 21st century, paired with $\overline{H_S^{ARR}}$ projected increases (decreases), enhanced for the extreme events. In the Indian Ocean, similar behavior was shown for SATL (SIND) events. At the three selected swell-arriving locations (P1, P2 and P3), it was shown that the projected changes for the conventional $\overline{H_S}$ tend to misrepresent the climate change signal which is propagated in different directions through swells from remote origins.

The unbalanced statistically significant projected changes in swell events $\overline{H_S^{ARR}}$, often showing opposite signals, are mostly compatible with those at the wave generation areas ($\overline{H_S^{OR}}$ and $\overline{U_{10}^{OR}}$). The $\overline{U_{10}^{OR}}$ projections are, in turn, consistent with a broader knowledge on future projected changes in the atmospheric regimes along the extratropical latitudes of both hemispheres (Collins *et al* 2013), the effects of which are shown to be felt far away in the tropical and subtropical latitudes. Additionally, both $\overline{\chi_{10}}$ (figure SM6a) and its associated extreme value frequency ($\chi_{10} > 5$; figure SM6b) were shown to be projected to increase in most of the global ocean, enhancing not only the swell impacts at the coast, but also in the open ocean, through repercussions on the MABL vertical wind profile (Högström *et al* 2009) and turbulence structure.

Our results share a new perspective on global wave climate projections, differing notably from the conventional $\overline{H_S}$ ones, unable to distinguish specific features from multiple incoming wave directions, critical for improved vulnerability assessments from the climate community. The direction of incoming swell waves plays a crucial role in wave-related impacts at the coast and offshore (Hemer *et al* 2008, Ranasinghe 2016, Harley *et al* 2017), often enhancing other climate change implications such as sea-level rise. Several areas of the global ocean were shown to be exposed to more than a single dominant swell wave direction, each associated to a different climate change signal. A directional approach on future wave climate studies, able to adequately represent the disproportionate flux of energy carried by swells propagating in multiple directions, is therefore recommended, to prevent potentially costly maladaptation to wave climate change, especially in the tropical and subtropical latitudes.

Data availability statement

The data that support the findings of this study are available upon reasonable request from the authors.

Acknowledgments

This work has been done under the auspices of the WMO supported COWCLIP (Coordinated Ocean Wave Climate Project). Gil Lemos is supported by the EarthSystems Doctoral School, at University of Lisbon, supported by Portuguese Foundation for Science

and Technology (FCT) project UIDB/50019/2020—Instituto Dom Luiz. Melisa Menendez acknowledges the financial support from the Ramon y Cajal Program (RYC-2014-6469) and project ECLISEA, part of ERA4CS/ERA-NET initiated by JPI Climate and cofounded by the European Union (Grant No. 690462). Mark Hemer acknowledges support of the Australian Commonwealth National Environmental Science Program Earth Systems and Climate Change Hub.

ORCID iDs

Gil Lemos https://orcid.org/0000-0002-2585-6871
Pedro M A Miranda https://orcid.org/0000-0002-4288-9456

References

Alves J H G M 2006 Numerical modeling of ocean swell contributions to the global wind wave climate *Ocean Model.* **11** 98–122

Amores A and Marcos M 2019 Ocean swells along the global coastlines and their climate projections for the twenty-first century *J. Clim.* **33** 185–99

Arblaster J M, Meehl G A and Karoly D J 2011 Future climate change in the southern hemisphere: competing effects of ozone and greenhouse gases *Geophys. Res. Lett.* **38** L02701

Ardhuin F, Chapron B and Collard F 2009 Observation of swell dissipation across oceans *Geophys. Res. Lett.* **36** L06607

Barnard P L *et al* 2015 Coastal vulnerability across the pacific dominated by El Niño/southern oscillation *Nat. Geosci.* **8** 801–7

Bengtsson L, Hodges K and Keenlyside N 2009 Will extratropical storms intensify in a warmer climate? *J. Clim.* **22** 2276–301

Bidlot J-R, Janssen P and Abdalla S 2005 A revised formulation for ocean wave dissipation in CY29R1 ECMWF Technical Memorandum, R60.9/JB/0(1) pp 1–35

Bitner-Gregersen E M, Eide L I, Hørte T and Vanem E 2015 Impact of climate change and extreme waves on tanker design SNAME Transactions 2014 USA

Chen G, Chapron B, Exraty R and Vandemark D 2002 A global view of swell and wind sea climate in the ocean by satellite altimeter and scatterometer *J. Atmos. Ocean. Technol.* **19** 1849–59

Collins M *et al* 2013 Long-term climate change: projections, commitments and irreversibility *Climate Change 2013: The Physical Science Basis. Contribution of Working Group I to the Fifth Assessment Report of the Intergovernmental Panel on Climate Change* ed T F Stocker, D Qin, G-K Plattner, M Tignor, S K Allen, J Boschung, A Nauels, Y Xia, V Bex and P M Midgley (Cambridge: Cambridge University Press) 107

Fan Y, Lin S-J, Griffies S M and Hemer M A 2014 Simulated global swell and wind-sea climate and their responses to anthropogenic climate change at the end of the twenty-first century *J. Clim.* **27** 3516–36

Grachev A A and Fairall C W 2001 Upward momentum transfer in the marine boundary layer *J. Phys. Oceanogr.* **31** 1698–711

Harley M D, Turner I L, Kinsela M A, Middleton J H, Mumford P J, Splinter K D, Phillips M S, Simmons J A, Hanslow D J and Short A D 2017 Extreme coastal erosion enhanced by anomalous extratropical storm wave direction *Sci. Rep.* **7** 6033

Harris D L 1966 The wave-driven wind *J. Atmos. Sci.* **23** 688–93

Hemer M A, Fan Y, Mori N, Semedo A and Wang X 2013 Projected changes in wave climate from a multi-model ensemble *Nat. Clim. Change* **3** 471–6

Hemer M A, Simmonds I and Keay K 2008 A classification of wave generation characteristics during large wave events on the Southern Australian margin *Cont. Shelf Res.* **28** 634–52

Hemer M A and Trenham C E 2016 Evaluation of a CMIP5 derived dynamical global wind wave climate model ensemble *Ocean Model.* **103** 190–203

Högström U, Sahleé E, Smedman A, Rutgersson A, Nilsson E, Kahma K K and Drennan W M 2015 Surface stress over the ocean in swell-dominated conditions during moderate winds *J. Atmos. Sci.* **66** 2764–79

Högström U, Smedman A, Sahleé E, Drennan W M, Kahma K K, Pettersson H and Zhang F 2009 The atmospheric boundary layer during swell: a field study and interpretation of the turbulent kinetic energy budget for high wave ages *J. Atmos. Sci.* **66** 2764–79

2014 IPCC-AR5 Climate Change 2014: The Physical Science Basis; (Cambridge: Cambridge University Press)

Jeffreys H 1924 On the formation of waves by wind *Proc. R. Soc.* A **107** 189–206

Jeffreys H 1925 On the formation of waves by wind II *Proc. R. Soc.* A **110** 341–7

Kinsman B 1965 *Wind Waves, Their Generation and Propagation on the Ocean Surface* (Englewood Cliffs, NJ: Prentice-Hall)

Lemos G, Menendez M, Semedo A, Camus P, Hemer M, Dobrynin M and Miranda P 2020 On the need of bias correction methods for wave climate projections *Glob. Planet. Change* **186** 103109

Lemos G, Semedo A, Dobrynin M, Behrens A, Staneva J, Bidlot J-R and Miranda P 2019 Mid-twenty-first century global wave climate projections: results from a dynamic CMIP5 based ensemble *Glob. Planet. Change* **172** 69–87

Lemos G, Semedo A, Dobrynin M, Menendez M and Miranda P 2020b Bias-corrected CMIP5-derived single-forcing future wind-wave climate projections toward the end of the twenty-first century *J. Appl. Meteorol. Climatol.* **59** 1393–414

Morim J *et al* 2019 Robustness and uncertainties in global multivariate wind-wave climate projections *Nat. Clim. Change* **9** 711–8

Munk W H, Miller G R, Snodgrass F E and Barber N F 1963 Directional recording of swell from distant storms *Phil. Trans. R. Soc.* A **255** 505–84

Pérez J, Méndez F J, Menéndez M and Losada I J 2014 ESTELA: a method for evaluating the source and travel time of the wave energy reaching a local area *Ocean Dyn.* **64** 1181–91

Portilla J 2012 Storm-source-locating algorithm based on the dispersive nature of ocean swells Avances-USFQ vol 4 pp C22–C36 (available at: www.usfq.edu.ec/publicaciones/avances/archivo_de_contenidos/Documents/volumen4/Avances2012vol4n1C22-C36.pdf)

Ranasinghe R 2016 Assessing climate change impacts on open sandy coasts: a review *Earth Sci. Rev.* **160** 320–32

Riahi K, Rao S, Krey V, Cho C, Chirkov V, Fischer G, Kindermann G, Nakicenovic N and Rafaj P 2011 RCP 8.5—a scenario of comparatively high greenhouse gas emissions *Clim. Change* **109** 33–57

Rutgersson A, Sætra Ø, Semedo A, Björn C and Kumar R 2009 Impact of surface waves in a regional climate model *Meteorol. Z.* **19** 247–57

Semedo A, Rutgersson A, Sterl A and Sušelj K 2012 The global wave age climate *Marine Engineering and Technology* ed Soares C G (London: Taylor and Francis Group) pp 539–43

Semedo A, Sætra Ø, Rutgersson A, Kahma K K and Pettersson H 2009 Wave induced wind in the marine boundary layer *J. Atmos. Sci.* **66** 2256–71

Semedo A, Sušelj K, Rutgersson A and Sterl A 2011 A global view on the wind sea and swell climate and variability from EERA-40 *J. Clim.* **24** 1461–79

Smedman A, Högström U, Bergström H, Rutgersson A, Kahma K K and Petterseon H 1999 A case study of air-sea interaction during swell conditions *J. Geophys. Res.* **104** 25833–51

Smedman A, Högström U, Sahleé E, Drennan W M, Kahma K K, Pettersson H and Zhang F 2009 Observational study of marine atmospheric boundary layer characteristics during swell *J. Atmos. Sci.* **66** 2747–63

Snodgrass F E, Groves G W, Hasselmann K F, Miller G R, Munk W H and Powers W M 1966 Propagation of swell across the Pacific *Philos. Trans. R. Soc.* A **259** 431–97

Sullivan P P, Edson J B, Hristov T and McWilliams J C 2008 Large-eddy simulations and observations of atmospheric marine boundary layers above nonequilibrium surface waves *J. Atmos. Sci.* **65** 1225–54

Tamarin T and Kaspi Y 2017 The poleward shift of storm tracks under global warming: a Lagrangean perspective *Geophys. Res. Lett.* **44** 10666–74

Toimil A, Losada I J, Nicholls R J, Dalrymple R A and Stive M J F 2019 Addressing the challenges of climate change risks and adaptation in 811 coastal areas: a review *Coast. Eng.* 103611

Tolman H 2009 User manual and system documentation of WAVEWATCH III version 3.14. NOAA/NWS/NCEP/MMAB technical note p 276

Wu Y, Ting M, Seager R, Huang H-P and Cane M 2010 Changes in storm tracks and energy transports in a warmer climate simulated by the GFDL CM2.1 model *Clim. Dyn.* **37** 53–72